Electronic Supplementary Material (ESI) for Energy & Environmental Science.


# Elucidating the Activity, Mechanism and Application of Selective Electrosynthesis of Ammonia from Nitrate on Cobalt phosphide

Shenghua Ye,† Zhida Chen,† Guikai Zhang, Wenda Chen Chao Peng, Xiuyuan Yang, Lirong Zheng*, Yongliang Li, Xiangzhong Ren, Huiqun Cao Dongfeng Xue*, Jieshan Qiu*, Qianling Zhang* and Jianhong Liu*

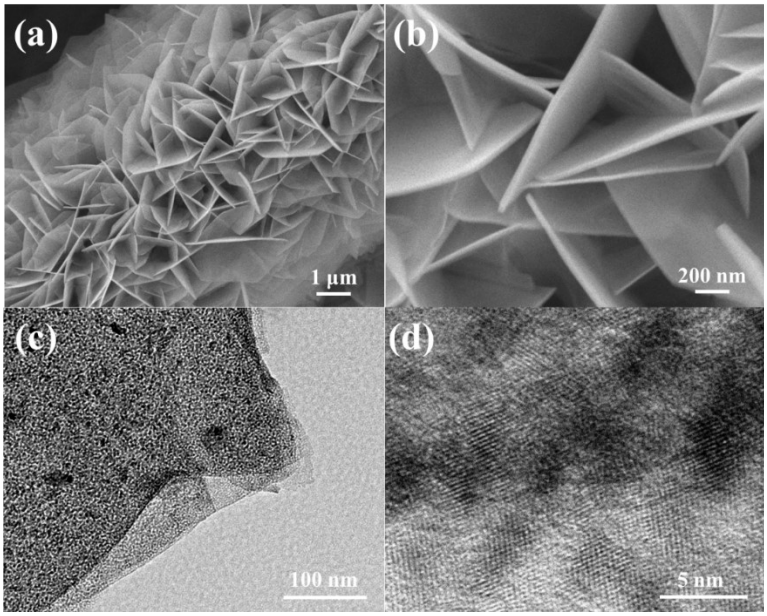


**Figure S1** (a, b) SEM and (c, d) TEM image of α-$Co(OH)_2$ NAs/CFC.

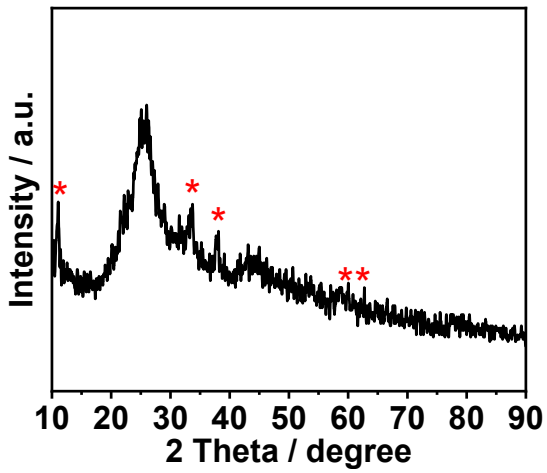


**Figure S2** XRD pattern of α-$Co(OH)_2$ NAs/CFC. [1-4]

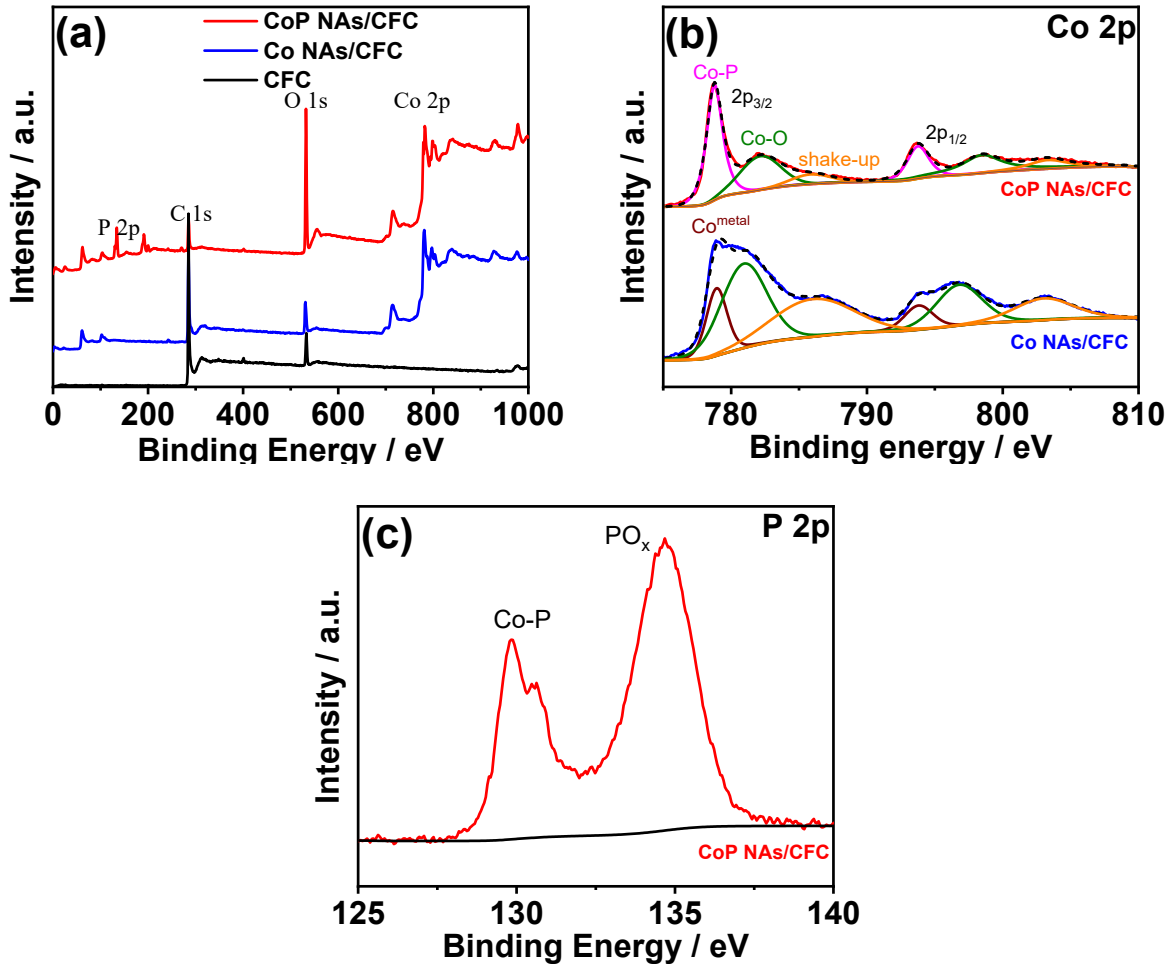


**Figure S3** XPS of (a) survey and (b) C1s of CoP NAs/CFC.

X-ray photoelectron spectroscopy (XPS) was implemented to further study the chemical and electronic state of Co and P. The surveys of CoP NAs/CFC and Co NAs/CFC were displayed in **Figure S3a**. The high-resolution Co 2p spectra of CoP NAs/CFC and Co NAs/CFC (**Figure S3b**) can be fitted. For CoP NAs/CFC, two peaks at 778.8 eV and 793.8 eV should be assigned to Co-P. The peaks at ~782.3 eV and ~798.6 eV assigned to $Co^{2+}$ accompanied by two satellite peaks are originated from inevitable surface oxidation created $CoO_x$ species. For Co NAs/CFC, metallic Co and $CoO_x$ species were also detected. With regard to P 2p spectra of CoP NAs/CFC, the signals of Co-P and P-$O_x$ also could be identified, which accords to the Co 2p spectra (**Figure S3c**).

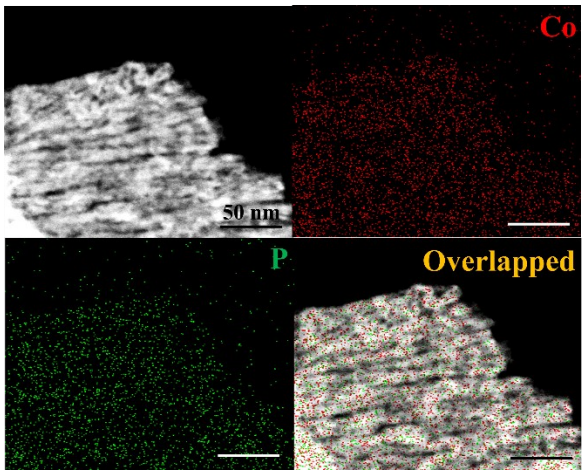


**Figure S4** HAADF-STEM image and corresponding elemental mapping of Co and P in CoP NAs/CFC

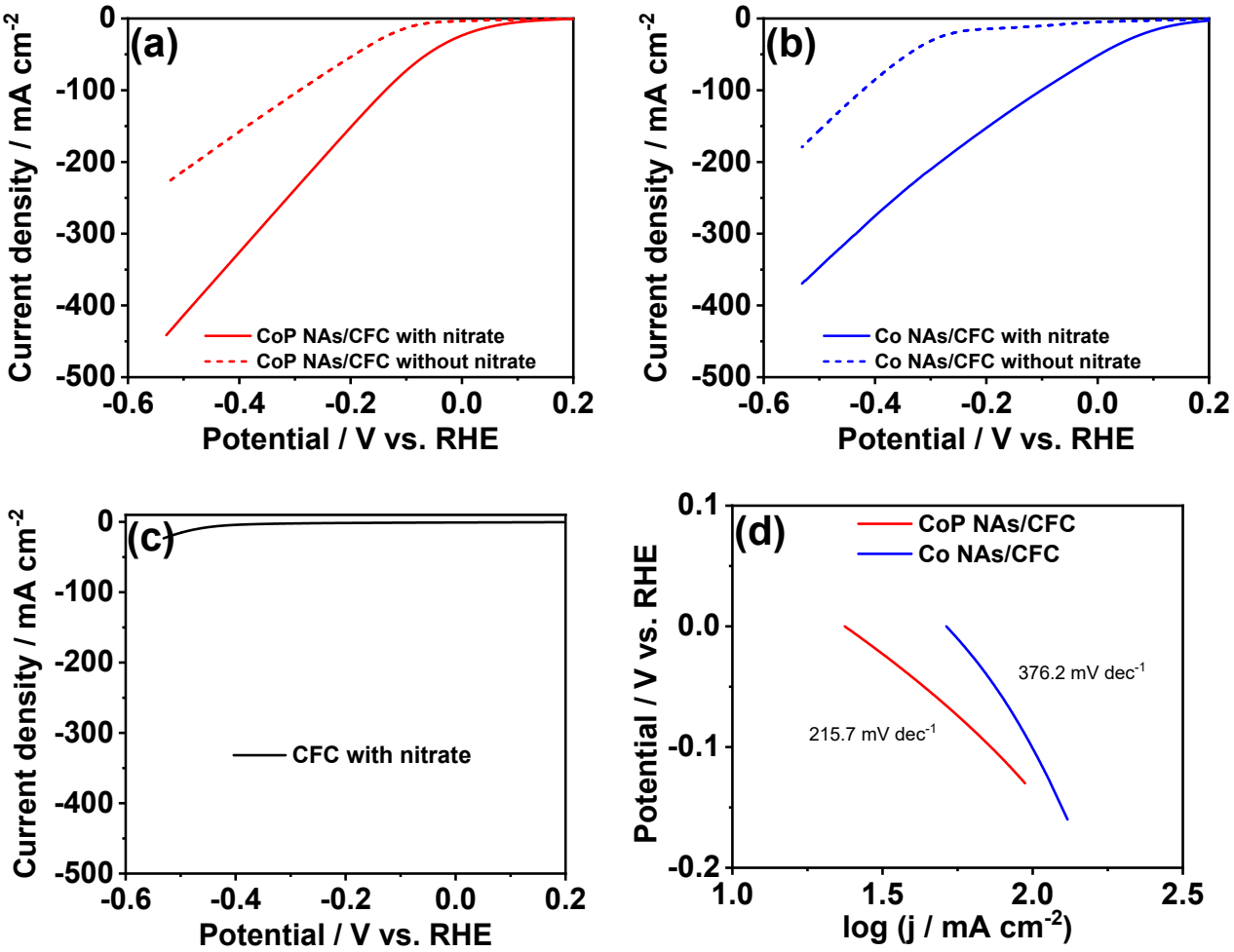


**Figure S5** LSV curves of (a) CoP NAs/CFC and (b) Co NAs/CFC in 1.0 M NaOH with and without 1.0 M $NaNO_3$ at scan rate of 5 mV/s without iR compensation; (c) LSV curves of CFC in 1.0 M $NaNO_3$ + 1.0 M NaOH at scan rate of 5 mV/s without iR compensation. (d) Tafel plots of CoP NAs/CFC and Co NAs/CFC in 1.0 M NaOH + 1.0 M $NaNO_3$.

The Tafel plot of CoP NAs/CFC was lower than that of Co NAs/CFC (**Figure S5d**), indicating that

they obeyed different rate-determining step. The lower Tafel slope renders CoP NAs/CFC presenting the larger catalytic current density at high overpotential, thus the current density of CoP NAs/CFC could surpass that of Co NAs/CFC.

The electrodynamic potential of $NO_3^-$ to $NO_2^-$ is calculated as follow:

$$NO_3^- + 3H^+ + 2e^- \rightarrow HNO_2 + H_2O \quad E_1^\theta = 0.93\,V \qquad ①$$

$$HNO_2 \leftrightarrow NO_2^- + H^+ \quad K_2^\theta = 4.6 \times 10^{-4} \qquad ②$$

$$H_2O \leftrightarrow H^+ + OH^- \quad K_3^\theta = 10^{-14} \qquad ③$$

$$NO_3^- + H_2O + 2e^- \rightarrow NO_2^- + 2OH^- \qquad ④$$

$$\log K_1^\theta = \frac{nE_1^\theta}{0.0591} \log E_1^\theta = \frac{2 \times 0.93}{0.0591} = 31.47$$

④=①+②+2③ $\Longrightarrow$ $\log K_4^\theta = \log K_{1+}^\theta \log K_{2+2}^\theta \log K_3^\theta = 31.47\text{-}3.34\text{-}2 \times 14 = 0.13$

$$E_{NO_3^-/NO_2^-}^\theta = E_4^\theta = \frac{0.059}{n} \log K_4^\theta = \frac{0.059}{2} \times 0.13 = 0.004\,V\ vs.\ SHE$$

$$\varphi_{RHE}(pH = 14) = -0.059pH = -0.059 \times 14 = -0.826\,V$$

$$E_{NO_3^-/NO_2^-}^\theta = 0.83\,V\ vs.\ RHE\ (pH = 14)$$

$$NO_3^- + 6H_2O + 8e^- \rightarrow NH_3 + 9OH^- \quad E_{NO_3^-/NH_3}^\theta = 0.69\,V\ vs.\ RHE\ (pH = 14) < E_{NO_3^-/NO_2^-}^\theta\ vs.\ RHE(pH = 14)$$

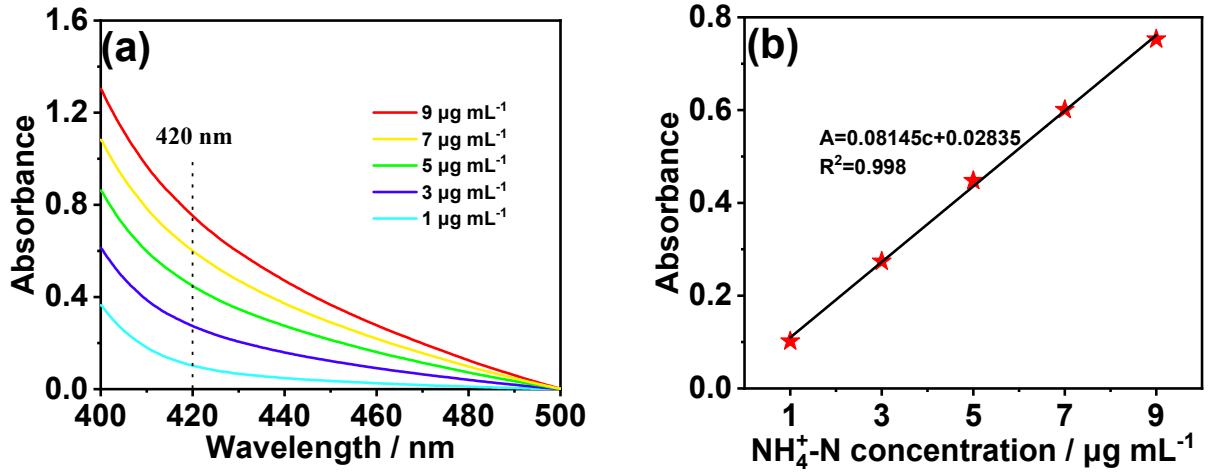


**Figure S6** (a) UV-Vis spectra of various $NH_3$ concentrations and (b) calibration curve used for estimating concentrations of $NH_3$.

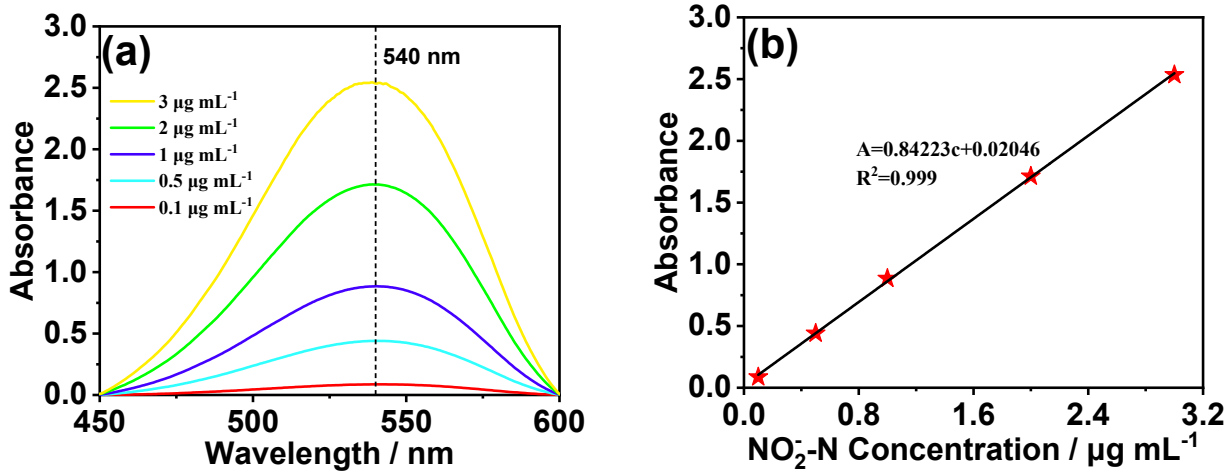


**Figure S7** (a) UV-Vis spectra of various $NO_2^-$ concentrations and (b) calibration curve used for estimating concentrations of $NO_2^-$.

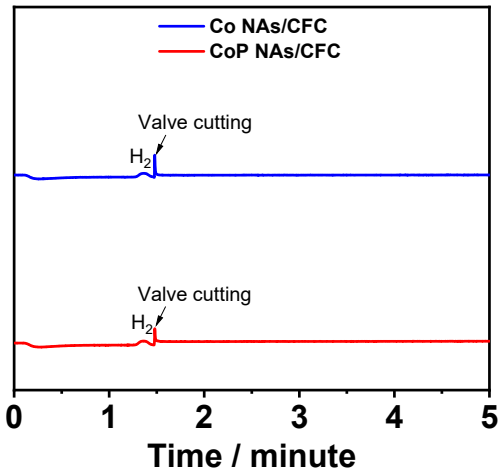


**Figure S8** Chromatograms for CoP NAs/CFC and Co NAs/CFC. None of $N_2$ were detected.

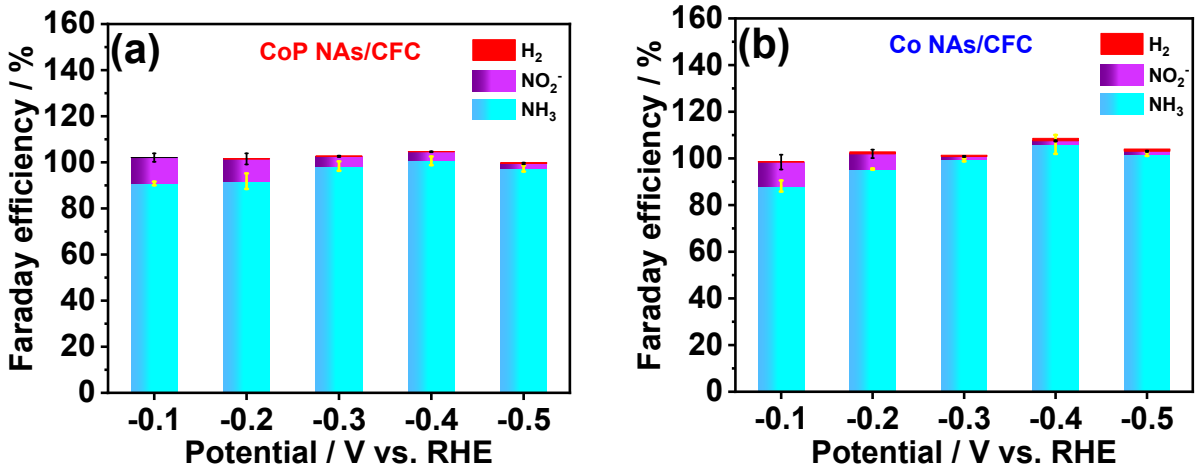


**Figure S9** Comparison of faradaic efficiency of $NH_3$(blue), $NO_2^-$ (purple) and $H_2$ (red) of (a) CoP NAs/CFC and (b) Co NAs/CFC at different potential (all the chronoamperometric tests were performed for 6 h, as shown in Figure 2a-b);

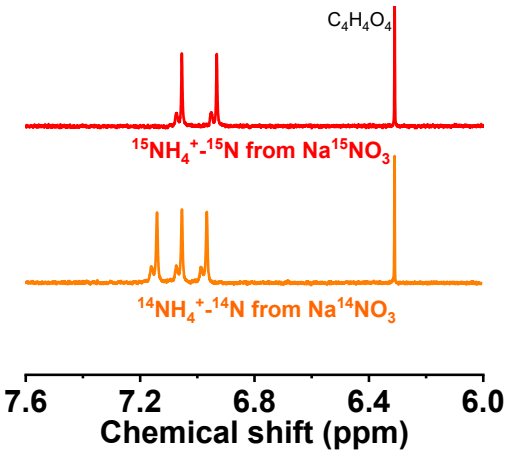


**Figure S10** $^{1}$H NMR spectra of ammonia after $NO_3^-$RR using $^{15}NO_3^-$ and $^{14}NO_3^-$ as nitrogen source over CoP NAs/CFC

As depicted in **Figure S10**, the $^{1}$H NMR (600 MHz) spectrum of electrolyte adopting $Na^{15}NO_3$ as reactant shows typical double peaks of $^{15}NH_3$, while the $^{1}$H NMR (600 MHz) spectra of electrolyte adopting $Na^{14}NO_3$ as reactant shows typical triple peaks of $^{14}NH_3$.[5] $^{15}$N isotope labeling experiment excluded the possible interference for ammonia detection.

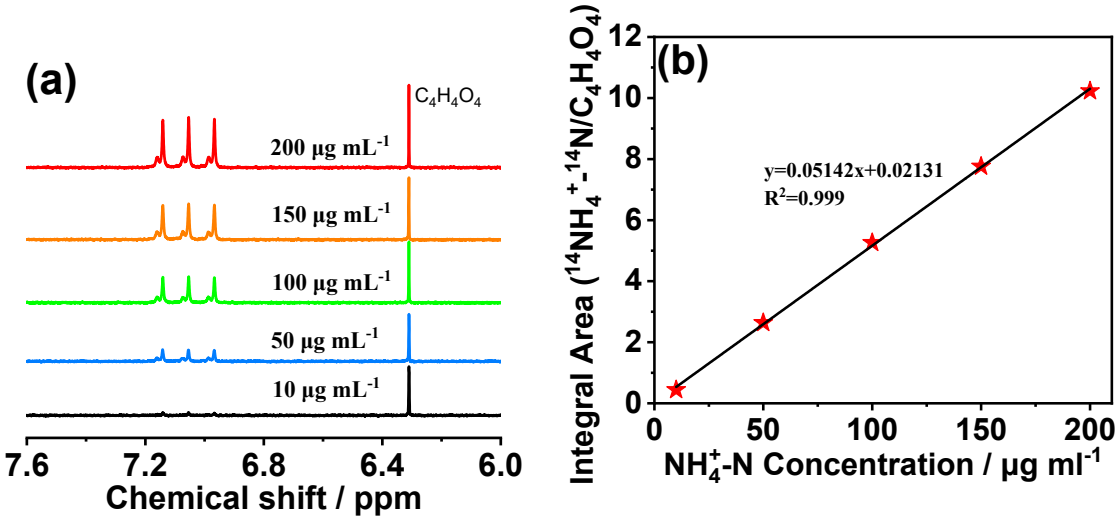


**Figure S11** (a) $^{1}$H NMR spectra (600 MHz) of standard samples of $(^{14}NH_4)_2SO_4$; (b) The standard curve of integral area ($^{15}NH_4^+$–$^{15}N/C_4H_4O_4$) against $^{15}NH_4^+$–$^{15}N$ concentration.

The yield of ammonia is quantified again by $^{1}$H NMR. As depicted in **Figure S11**, utilizing the peak area of $^{1}$H NMR to quantify the concentration of ammonia in electrolytes, the results were very close to

that of colorimetric methods (**Figure S12**), proving the accuracy of quantitative methods.

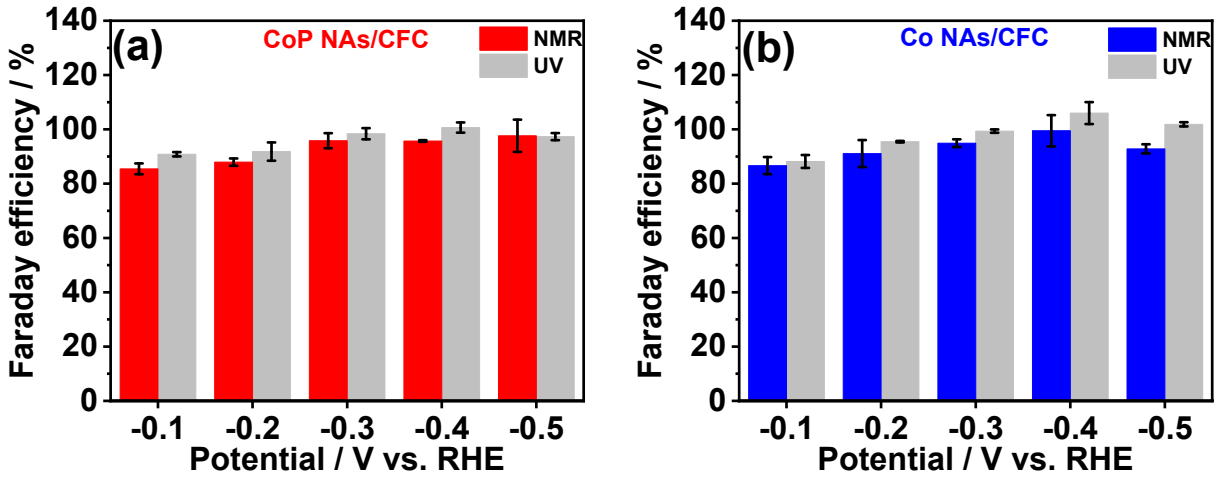


**Figure S12** Comparison of the FE for ammonia of (a) CoP NAs/CFC and (b) Co NAs/CFC measured by UV-Vis spectra and $^{1}$H NMR.

The FE calculated by $^{1}$H NMR are slightly lower than those calculated by UV-Vis spectra, this phenomenon may be attributed to the accuracy differences between two methodologies, but their tendencies are almost compatible.

**Table 1** Comparison of $NO_3^-$RR activity and $NH_3$ production performance between CoP NAs/CFC, recently-reported electrocatalysts and Harber-Bosch process.

| Materials | $NO_3^-$ concentration | Electrolyte | FE($NH_3$) | Ammonia-evolving rate | Ref. |
|---|---|---|---|---|---|
| **CoP NAs/CFC** | 1.0 M | 1.0 M NaOH | ~100% at -0.3 V vs. RHE | 9.56 mol $h^{-1}$ $m^{-2}$ / 16252 μg $h^{-1}$ $cm^{-2}$/ 0.569 mol $g_{cat}^{-1}$ $h^{-1}$ | This work |
| **Fe- and Ru-based materials (Haber-Bosch process)** | - | - | - | < 0.2 mol $g_{cat}^{-1}$ $h^{-1}$ | Z. Elektrochem. Angew. Phys.Chem. **1913**, 19, 53; Angew. Chem. Int. Ed. **2013**, 52, 12723 |
| **PTCDA/O-Cu** | 500 ppm | 0.1 M PBS | 77 ± 3% at -0.4 V | 436 ± 85 μg $h^{-1}$ $cm^{-2}$ / 0.256 ± 0.005 mol $h^{-1}$ $m^{-2}$ | Nat. Energy **2020**, 5, 605-613 |
| **Ru-ST-12** | 1.0 M | 1 M KOH | 100% at -0.2 V vs. RHE | 11.7 ± 0.04 mol $h^{-1}$ $m^{-2}$ | J. Am. Chem. Soc. **2020**, 142, 7036-7046 |
| **$Cu/Cu_2O$ nanowire arrays** | 200 ppm | 0.5 M $Na_2SO_4$ | 95.8% at -0.85 V vs. RHE | 2.449 mol $h^{-1}$ $m^{-2}$ | Angew. Chem., Int. Ed. **2020**, 59, 5350-5354 |
| **$TiO_2$ nanotubes with oxygen vacancies** | 50 ppm | $Na_2SO_4$ | 85% at -1.6 V vs. SCE | 0.045 mol $g_{cat}^{-1}$ $h^{-1}$ | ACS Catal. **2020**, 10, 3533-3540 |
| **$Cu_{50}Ni_{50}$ alloy** | 0.1 M | KOH | ~ 99±1 % at -0.2 V vs. RHE | - | J. Am. Chem. Soc. **2020**, 142, 5702-5708 |
| **Ti foil** | 0.4 M | 0.1 M $HNO_3$ | 82% at -1 V vs. RHE | - | ACS Sustainable Chem. Eng. **2020**, 8, 2672-2681 |
| **Fe-PPy SACs** | 0.1 M | 0.1 M KOH | 100% at -0.6 V vs. RHE | 1.187 mol $h^{-1}$ $m^{-2}$ | Energy&Environ. Sci., **2021**, DOI: 10.1039/D1EE00545F |
| **Au/C** | 1.0 mM | 0.5 M $K_2SO_4$ | 26% at -0.3 V vs. RHE | 0.0158 mol $h^{-1}$ $m^{-2}$ | ACS Energy Lett. **2020**, 5, 2095-097 |
| **Cu nanosheet** | 10 mM | 0.1 M KOH | 99.7% at -0.15 V vs. RHE | 0.0229 mol $g_{cat}^{-1}$ $h^{-1}$ | Appl. Mater. Today **2020**, 19, 100620. |

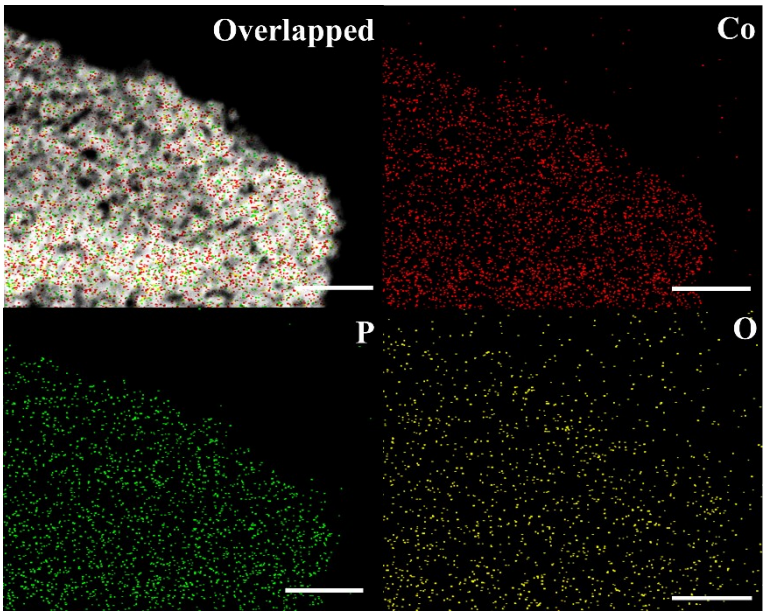


**Figure S14** TEM image and corresponding EDS mapping of CoP NAs/CFC after 6 h $NO_3^-$RR.

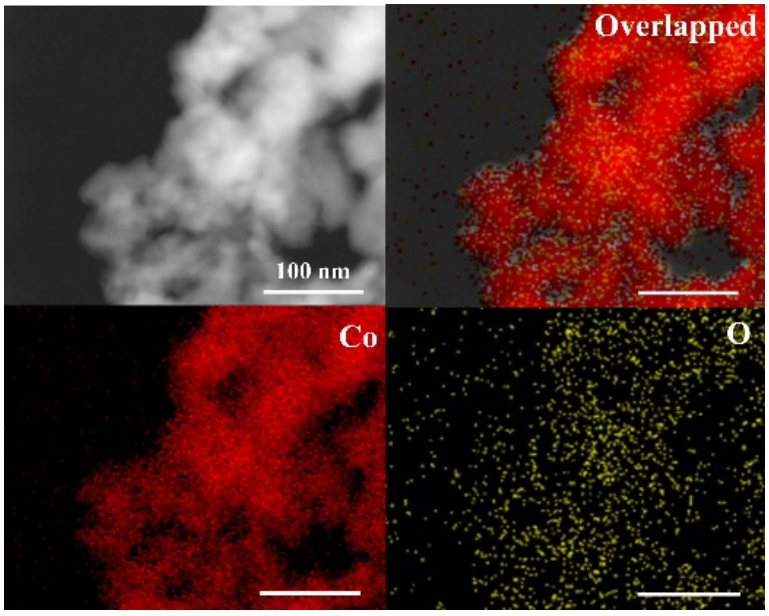


**Figure S15** TEM image and corresponding EDS mapping of Co NAs/CFC after 6 h $NO_3^-$RR.

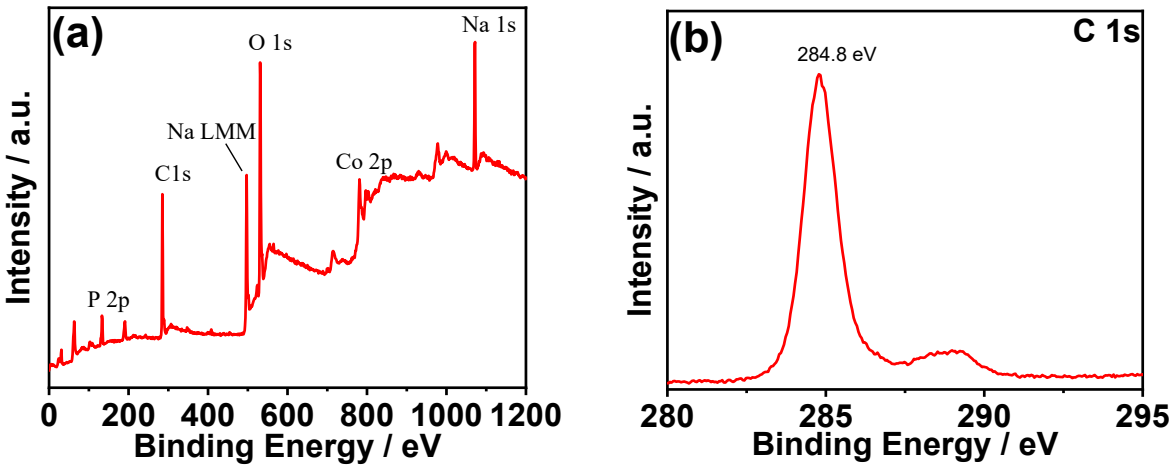


**Figure S16** XPS of (a) survey and (b) C1s of CoP NAs/CFC after 6 h $NO_3^-$RR.

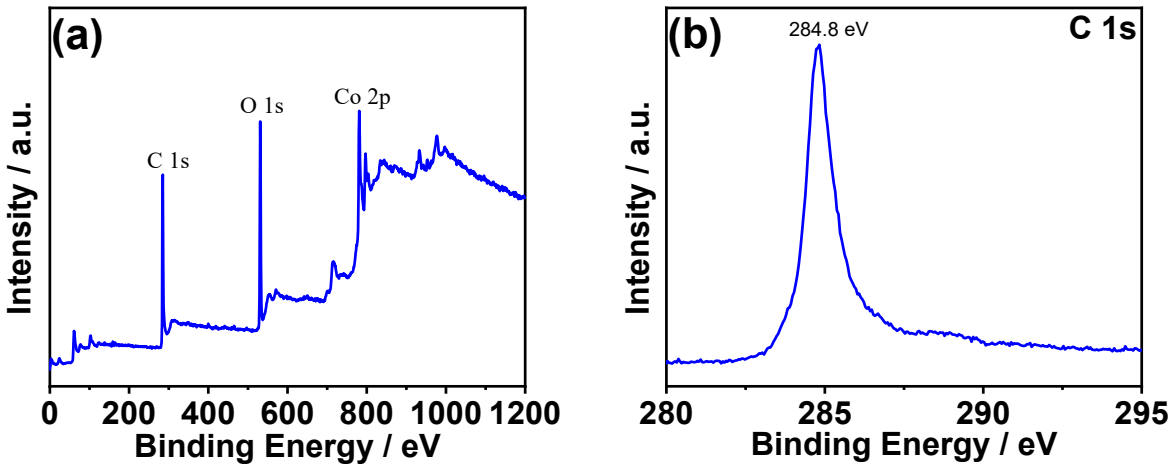


**Figure S17** XPS of (a) survey and (b) C1s of Co NAs/CFC after 6 h $NO_3^-$RR.

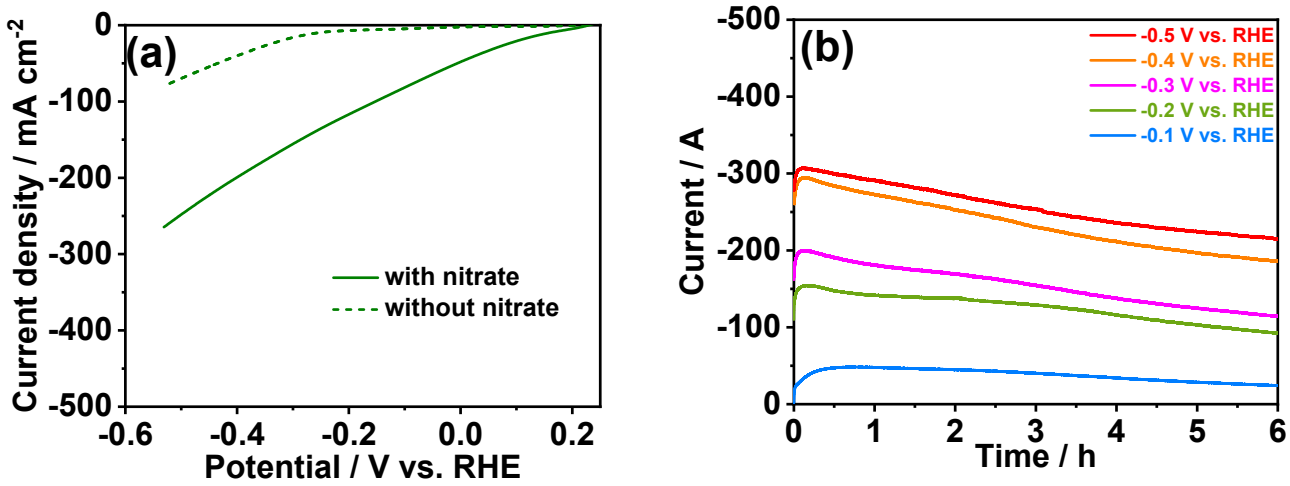


**Figure S18** (a) Liner sweep voltammetry curves of $Co(OH)_2$ NAs/CFC in 1.0 M NaOH with (solid line) and without (dotted line) 1.0 M nitrate; (b) Chronoamperometric curves of $Co(OH)_2$ NAs/CFC on different potential for 6 h.

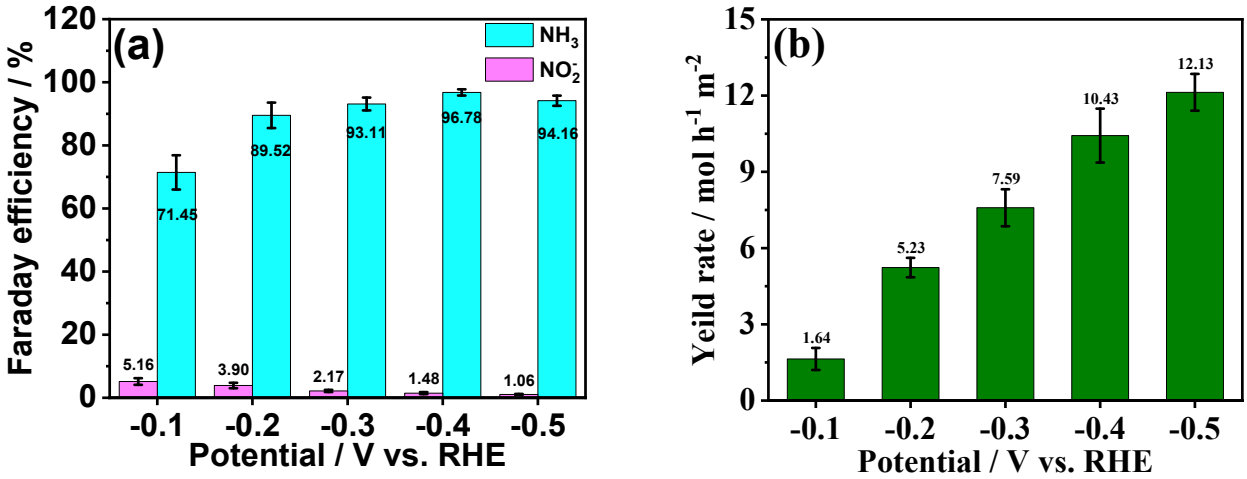


**Figure S19** (a) Comparison of faradaic efficiency of $NH_3$ (blue) and $NO_2^-$ (purple) of $Co(OH)_2$ NAs/CFC at different potential (all the chronoamperometric tests were performed for 6 h); (b) Summarized total ammonia-evolving rates of $Co(OH)_2$ NAs/CFC obtained from 6 h catalysis at different potential. (Error bars was derived from experimental results from three independent samples).

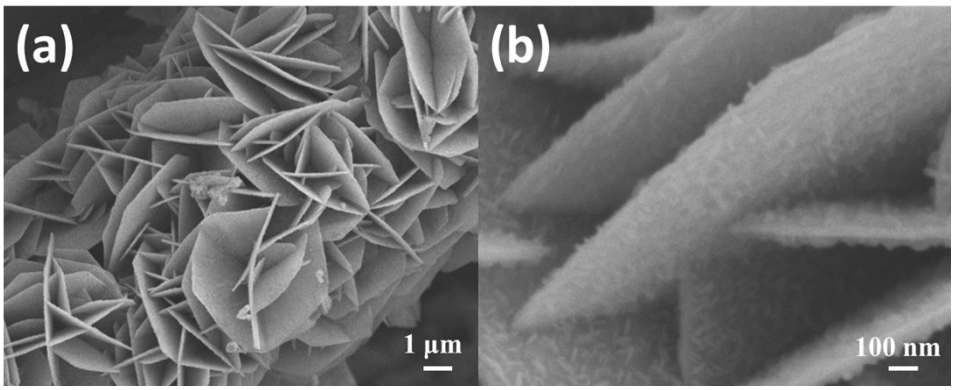


**Figure S20** SEM images of $Co(OH)_2$ NAs/CFC after 6h $NO_3^-$RR

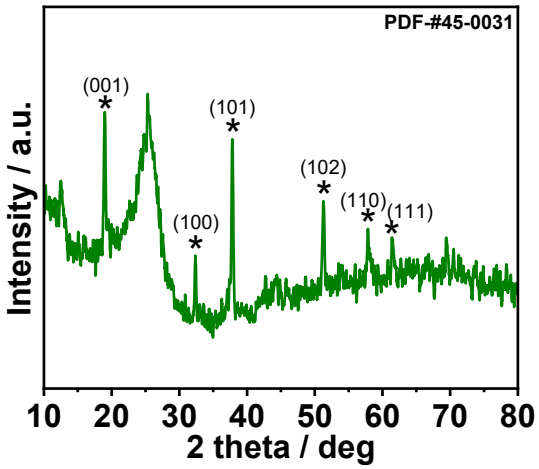


**Figure S21** XRD pattern of $Co(OH)_2$ NAs/CFC after 6h $NO_3^-$RR

The stability and yield rate of ammonia for $Co(OH)_2$ NAs/CFC are shown in **Figure S18-19**. **Figure S20** suggests that the morphology of $Co(OH)_2$ NAs/CFC slightly varied after long-term test. **Figure S21** suggests that $Co(OH)_2$ transformed from α-phase to β-phase during $NO_3^-$RR, and β-$Co(OH)_2$ is the real catalytic species. The catalytic performances of β-$Co(OH)_2$ are similar to those of Co NAs/CFC, but much inferior to those of CoP NAs/CFC.

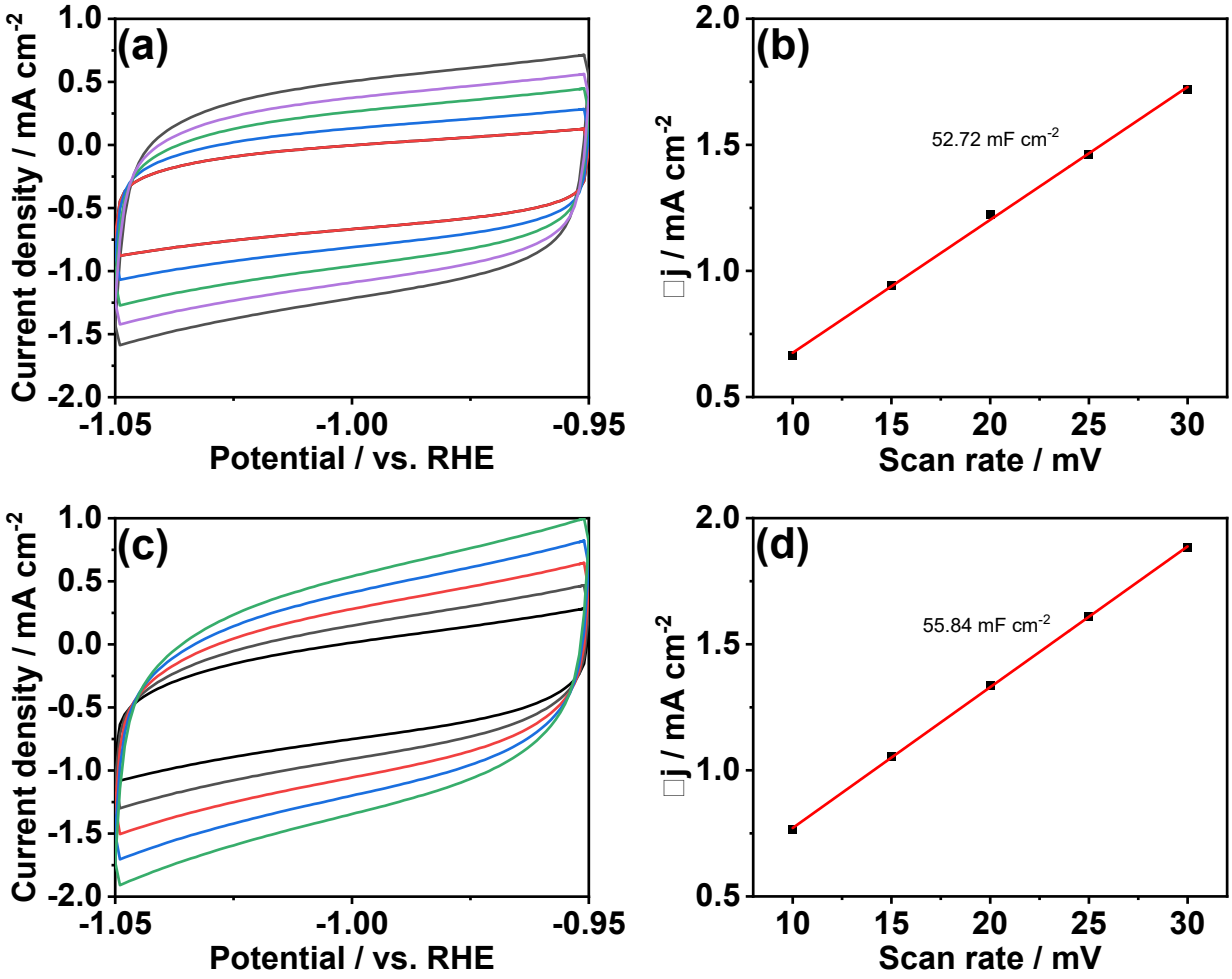


**Figure S22** CV curves of CoP NAs/CFC (a) before and (c) after $NO_3^-$RR respectively, (b and d) corresponding current density variation plotted against the scan rate, fitted to a linear regression, enables the estimation of the double-layer capacitance ($C_{dl}$).

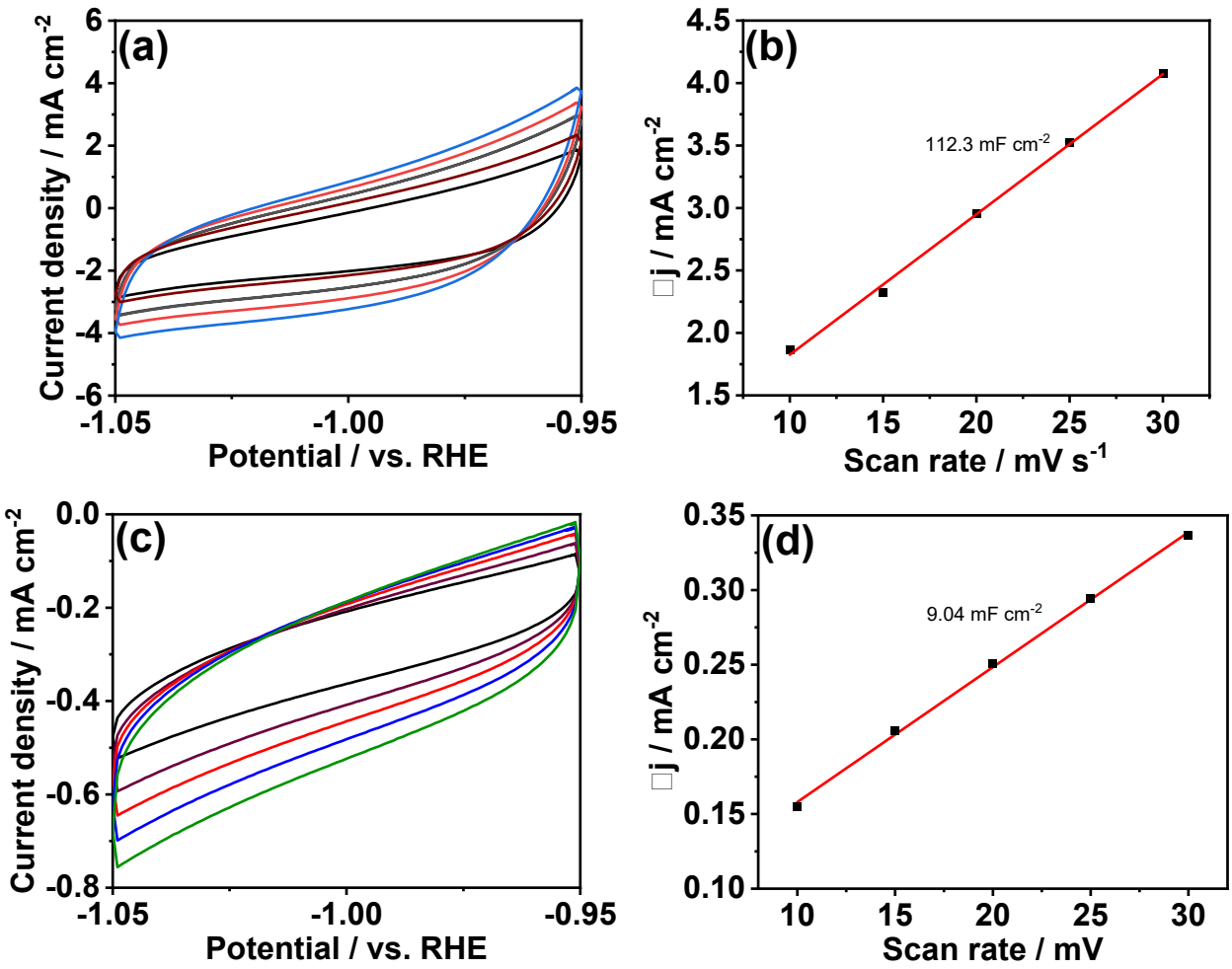


**Figure S23** CV curves of Co NAs/CFC (a) before and (c) after $NO_3^-$RR respectively, (b and d) corresponding current density variation plotted against the scan rate, fitted to a linear regression, enables the estimation of the double-layer capacitance ($C_{dl}$).

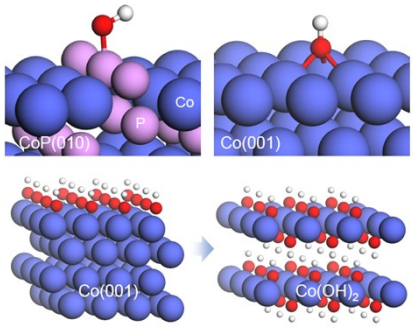


**Figure S24** The projected density of states (DOSs) of OH adsorption at the P site of CoP(010) surface.

The adsorption of OH species were investigated at the active sites on both CoP (010) and Co (001) surfaces (**Figure S24**). The adsorption energy is -2.59 eV for OH adsorbing at the exposed Co site on the CoP (010) surface, while that at the P site is -2.62 eV that shows even more favorable thermodynamics.

The density of states (DOSs) also indicates the strong p orbital interaction between OH and P site in the valence band of CoP (010), which is consistent with the favorable binding energy (**Figure S25**). In the presence of electrolyte (1.0 M NaOH and 1.0 M $NaNO_3$), the P site receives a higher coverage of OH species than the Co site on the CoP (010) surface. In contrast, OH adsorption energy becomes as low as -3.18 eV at the Co site on the Co (001) surface, which is 0.56 eV lower in magnitude than its adsorption on the CoP (010) surface, implying the much stronger binding of O(H)-Co on the Co (001) surface. The more favorable adsorption energy increases the coverage of OH species on the Co (001) surface relative to the CoP (010) and might drive the formation of $Co(OH)_2$.

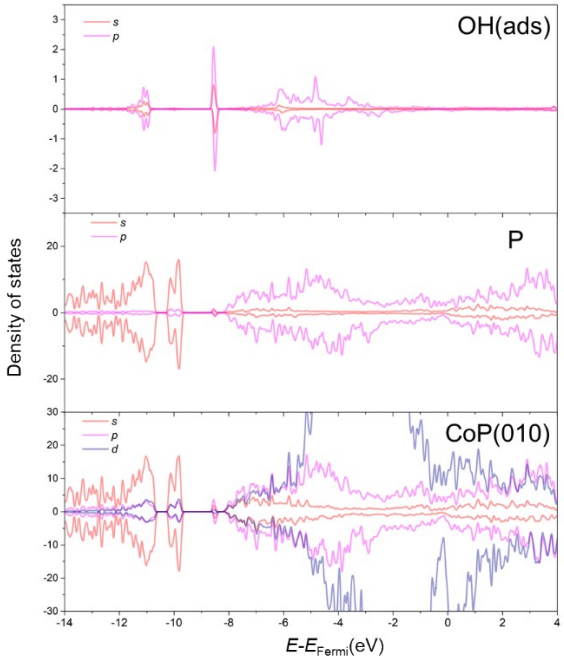


**Figure S25** The projected density of states (DOSs) of OH adsorption at the P site of CoP (010) surface.

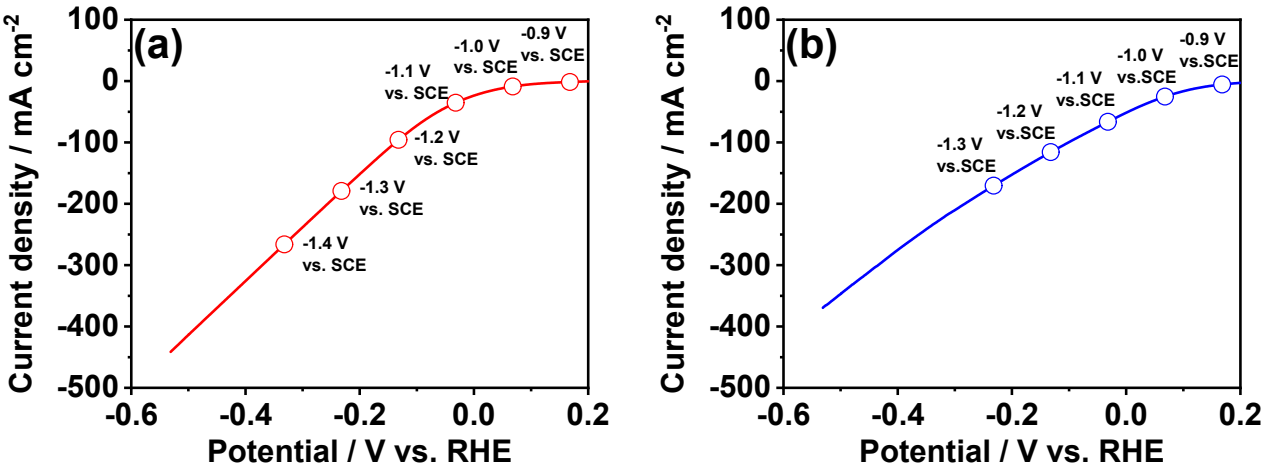


**Figure S26** LSV curve of (a) CoP NAs/CFC, (b) Co NAs/CFC and corresponding selected potentials for operando XANES.

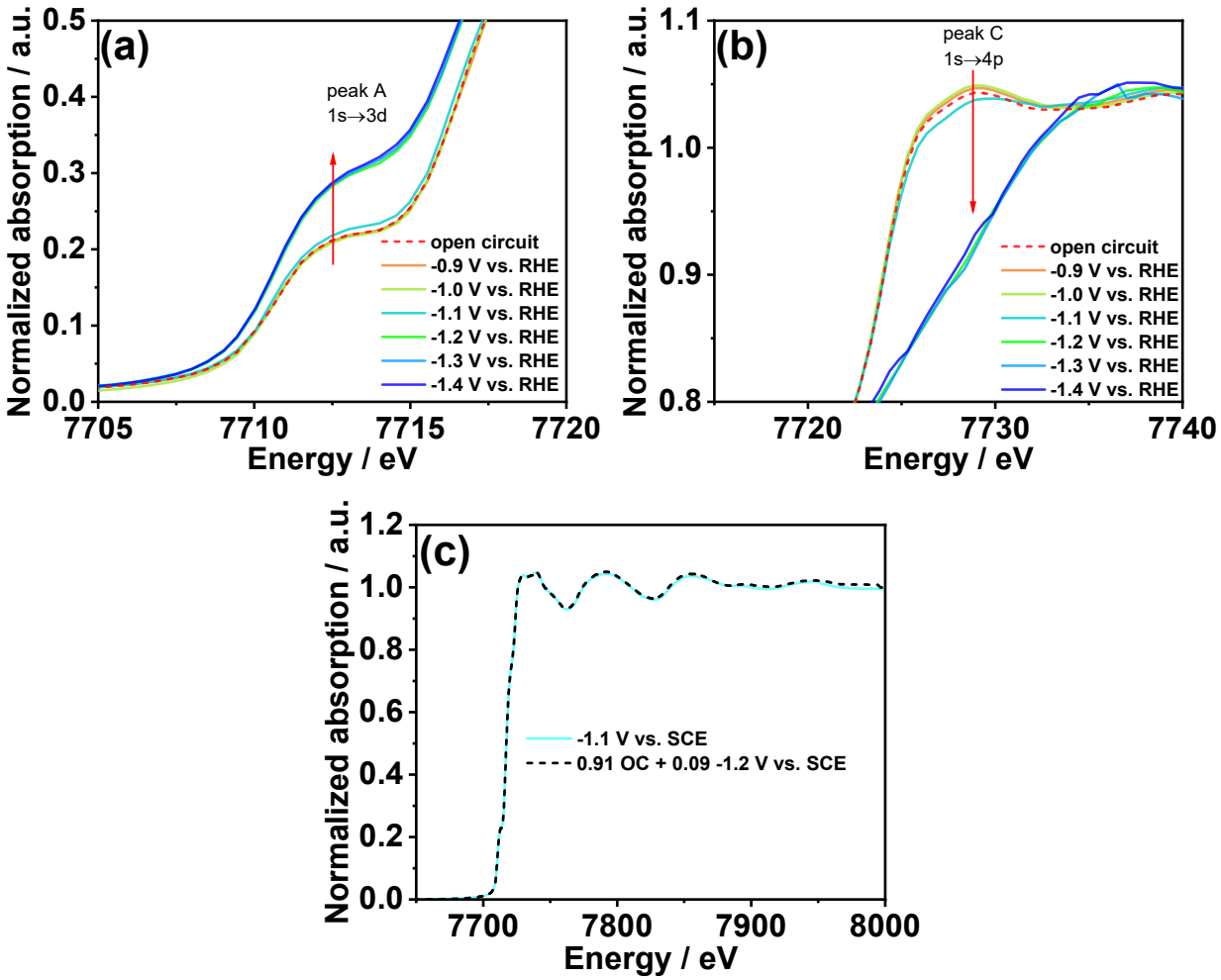


**Figure S27** Variation of (a) peak A and (b) peak C at white line versus applied potential; (c) LCF analysis of the data at -1.1 V vs. SCE.

As depicted in **Figure S27a-b**, the white line characteristic remained unchanged until the applied potential was lowered than -1.1 V vs. SCE which implies the trigger of $NO_3^-$RR for CoP NAs/CFC, in which peak A was enhanced while peak C was weakened simultaneously. For the curves at -1.1 V vs. SCE, the variation began to appear. Linear combination fitting (LCF) analysis suggests that the curves at -1.1 V vs. SCE can be fitted by 91% of OC and 9% of -1.2 V vs. SCE. When the cathodic potential was further decreased, XANES of Co K-edge kept stable.

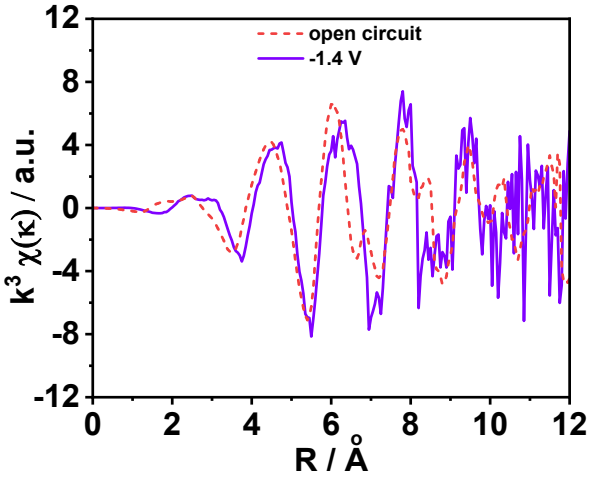


**Figure S28** EXAFS of Co K-edge of CoP NAs/CFC.

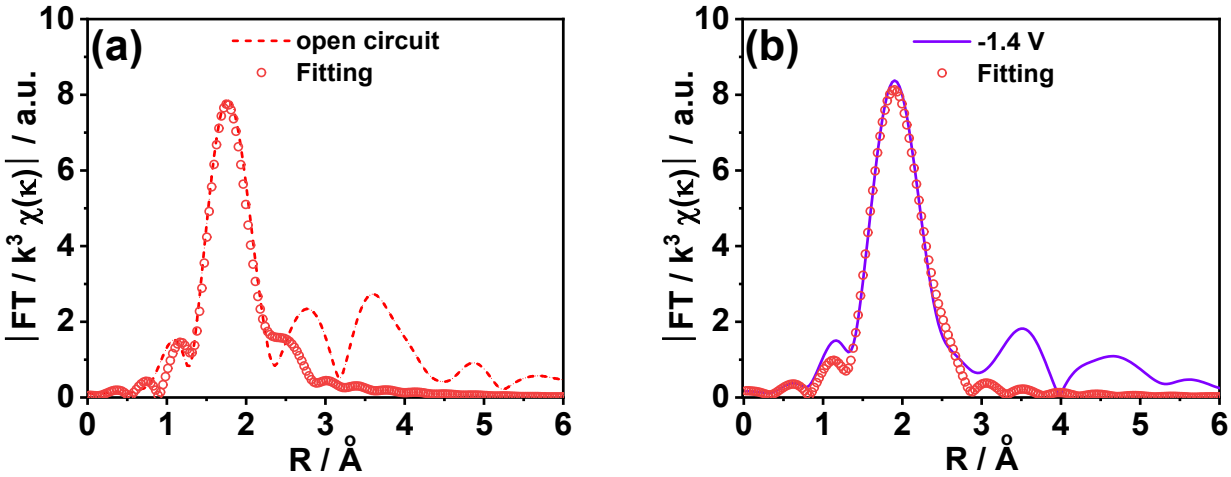


**Figure S29** Fitting of FT-EXAFS of Co K-edge of Co NAs/CFC at (a) open circuit and (b) -1.4 V.

**Table 2** The EXAFS fitting parameters at the Co K-edge for CoP NAs/CFC.

| Sample | Shell | N [a] | R (Å) [b] | $\sigma^2$ (Å$^2$·10$^{-3}$) [c] |
|---|---|---|---|---|
| **Open circuit** | Co-P | 2.95 | 2.246 | 3.0 |
| | Co-Co | 1.47 | 2.596 | 5.1 |
| **-1.4 V vs. SCE** | Co-P | 2.41 | 2.257 | 1.4 |
| | Co-Co | 1.40 | 2.567 | 2.3 |

[a]*N*: average coordination numbers; [b]*R*: bond distance; [c] $\sigma^2$: Debye–Waller factors; [d] $\Delta E_0$: the inner potential correction; *R* factor: goodness of fit. The *S*02 was set as 0.749 for Co-Co.

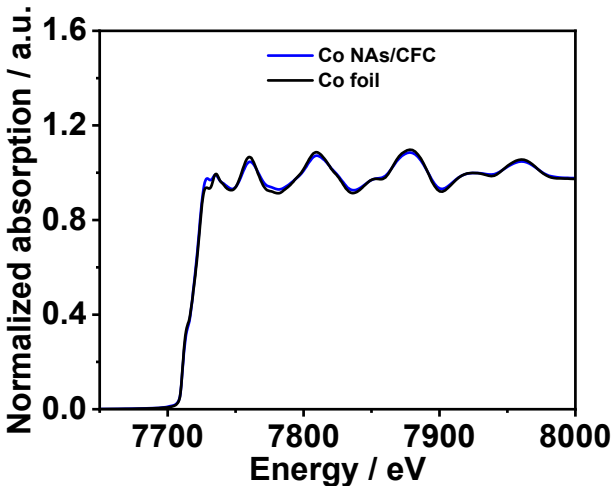


**Figure S30** XANES of Co K-edge of Co NAs/CFC and Co foil.

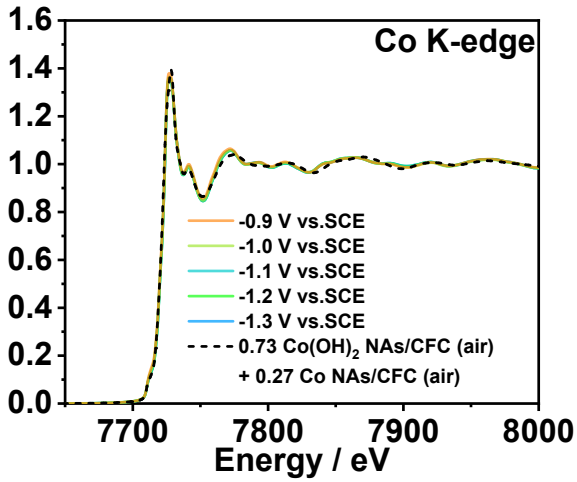


**Figure S31** Operando XANES of Co K-edge of Co NAs/CFC at potential of -0.9, -1.0, -1.1, -1.2 and -1.3 V vs. SCE, and LCF analysis.

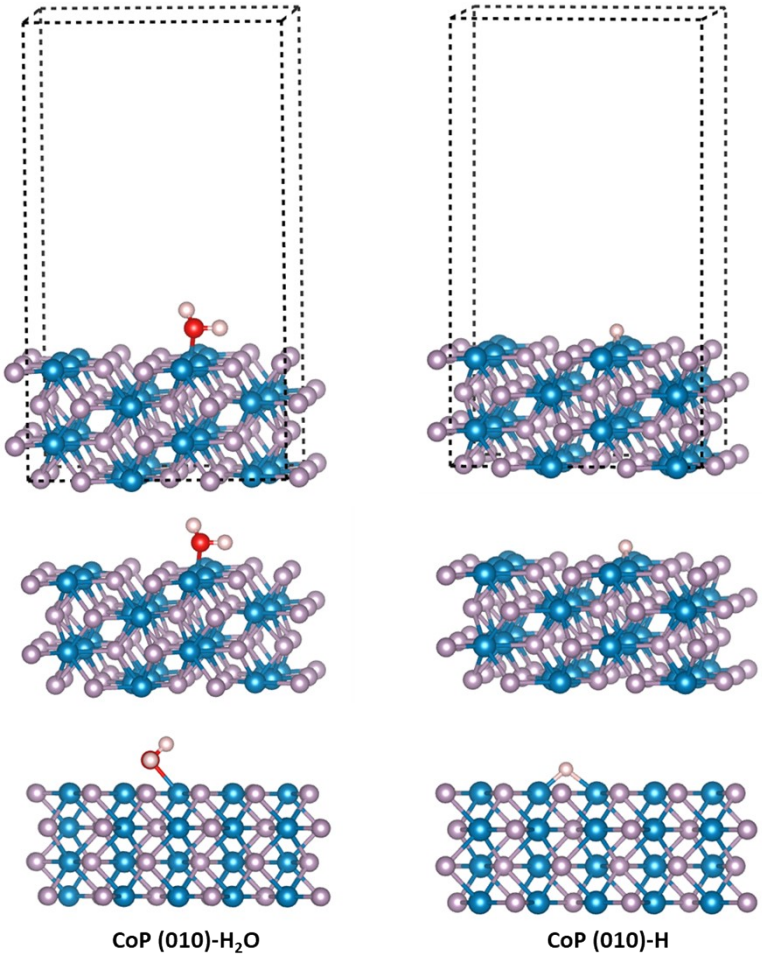


**Figure S32** The water dissociation on the model of CoP.

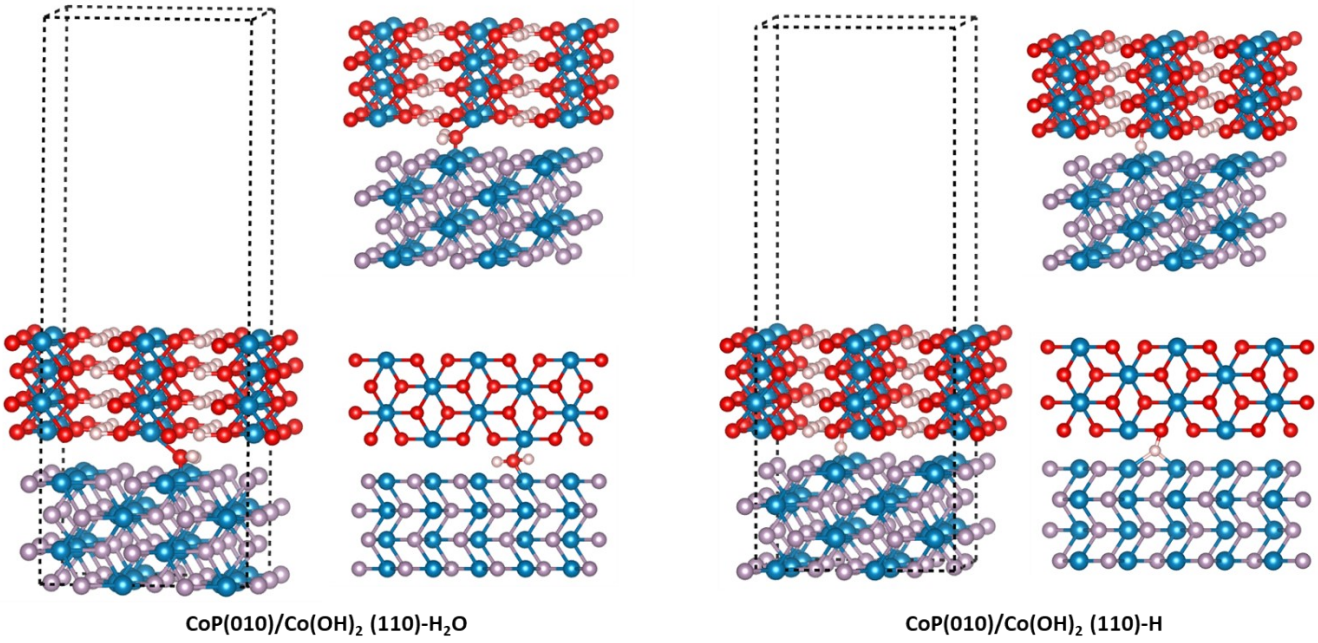


**Figure S33** The water dissociation on the model of CoP/$Co(OH)_2$.

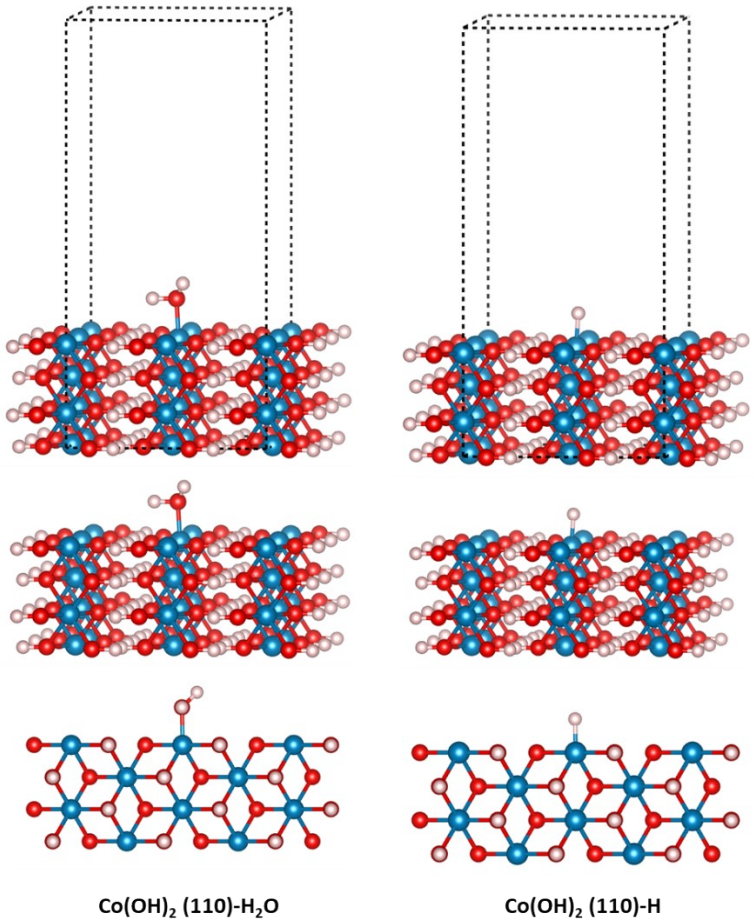


**Figure S34** The water dissociation on the model of $Co(OH)_2$.

Reference

1. L. Poul; N. Jouini; F. Fie´vet. *Chem. Mater*. 2000, ***12***, 3123-3132.
2. S. H. Ye, Z. X. Shi, J. X. Feng, Y. X. Tong and G. R. Li, *Angew. Chem. Int. Ed.* 2018, **57**, 2672-2676.
3. S. Ye, Y. Zhang, W. Xiong, T. Xu, P. Liao, P. Zhang, X. Ren, C. He, L. Zheng, X. Ouyang, Q. Zhang and J. Liu, *Nanoscale*, 2020, **12**, 11079-11087.
4. S. Ye, W. Xiong, P. Liao, L. Zheng, X. Ren, C. He, Q. Zhang and J. Liu, *J. Mater. Chem. A*, 2020, **8**, 11246-11254.
5. Y. Wang, W. Zhou, R. Jia, Y. Yu and B. Zhang, *Angew. Chem. Int. Ed.* 2020, **59**, 5350-5354.